(Received 28 October 2025, Accepted 8 December 2025, Scheduled 18 December 2025)

A Novel Wideband Coaxial-to-Rectangular Waveguide Transition Integrated with a Septum Horn Antenna for C-Band Satellite

Ajitesh and Manoj K. Meshram*

Department of Electronics Engineering, Indian Institute of Technology (BHU), Varanasi 221005, India

ABSTRACT: In this paper, a novel wideband coaxial-to-rectangular waveguide transition integrated with a septum horn antenna is proposed for C-band satellite communication applications. The design employs a modified supershape excitation probe, derived from an extended superformula, to achieve smooth impedance transformation and broadband performance. Initially, the probe geometry is optimized through parametric simulations to validate its effectiveness within a rectangular waveguide structure. The transition is then effectively incorporated into a stepped septum horn antenna that facilitates dual circular polarization through a compact dual-feed mechanism. The septum structure ensures efficient conversion of linearly polarized modes into left-hand and right-hand circularly polarized waves, while maintaining high isolation and low axial ratio. An equivalent circuit model is developed to provide analytical insight into the impedance behavior. A prototype antenna is fabricated, and its performance is validated through measurements. The measured results confirm reflection coefficients below −10 dB across 4.6–8.6 GHz, peak gain of 15.8 dBi, and inter-port isolation exceeding 20 dB. Furthermore, the antenna achieves a 3 dB axial ratio bandwidth of 76.9%. A comparison with state-of-the-art designs demonstrates the superior performance and design efficiency of the proposed antenna architecture.

1. INTRODUCTION

In recent years, satellite communication systems have increasingly required high-capacity, wideband, and reliable performance to support growing data demands in modern applications. Among the various frequency bands, the C-band has become a preferred choice due to its strong resistance to atmospheric effects and favorable propagation characteristics [1–3]. These features make it especially suitable for applications such as television broadcasting, telemetry, remote sensing, and secure communication links. To meet system performance requirements in such environments, antenna subsystems must offer wide impedance bandwidth, high gain, and stable circular polarization (CP) to combat polarization mismatch and multipath fading inherent in satellite links [4, 5].

A fundamental component within these systems is coaxial-to-rectangular waveguide transition, which enables efficient energy transfer between coaxial feeds and waveguide-based antennas [6, 7]. Traditional designs — such as stepped, tapered, or standard cylindrical probes — often suffer from limited impedance bandwidth due to abrupt discontinuities and insufficient adaptability for fine-tuning impedance transformation. Alternatively, CP can be realized without complex transitions using truncated-aperture single-feed horns; however, the 3-dB axial-ratio bandwidth is limited (≈ 26%) [8]. These challenges become more significant in systems requiring dual CP capability, as such systems demand low reflection coefficients, high inter-port isolation, and stable broadband radiation characteristics. Achieving these simultaneously within a compact and manufacturable structure remains a persistent design challenge in satellite antenna engineering [9–18].

To overcome these limitations, various methods have been explored. Simple cylindrical probes, though widely used, inherently restrict bandwidth and fail to support modern wideband specifications. Alternative schemes, such as ridge-loaded transitions, dielectric loading, multi-step thickness and multi-step transitions, offer modest improvements but often lead to increased insertion loss, mechanical complexity, or fabrication sensitivity [19–23]. Likewise, septum horn antennas are commonly employed for generating dual CP due to their ability to convert orthogonal linear modes into left-hand and right-hand circular polarization. However, conventional implementations frequently face trade-offs between bandwidth, polarization purity, and design simplicity, making them less suitable for tightly integrated wideband satellite systems [24].

Recent research has sought to enhance circular polarization (CP) performance by modifying probe geometries and septum profiles, incorporating features such as corrugated horns, asymmetric feeds, and tuning structures [25–27]. While these techniques offer some improvements, they tend to complicate fabrication and often require extensive optimization to ensure consistent performance across the C-band. Asymmetric linear-tapered horn geometries have also been introduced to support dual-band CP operation, although they typically exhibit constrained bandwidth and reduced flexibility for integration [28].

* Corresponding author: Manoj Kumar Meshram (mkmeshram.ece@iitbhu.ac.in).

More recently, horns employing twisted internal ridges shaped by the Gielis superformula have achieved notable improvements in axial-ratio bandwidth and CP stability, yet involve increased geometrical complexity and additional manufacturing constraints [29]. Despite these developments, a clear gap remains in realizing a unified feed and radiator structure that simultaneously provides broad impedance bandwidth, low inter-port coupling, high CP purity, and compactness for satellite terminals [30–33], including prior work on supershape-based transition designs [34].

In this work, a novel wideband coaxial-to-rectangular waveguide transition is proposed, featuring a modified supershape excitation probe derived from an extended superformula and integrated within a stepped septum horn antenna tailored for C-band satellite communication systems. The supershape probe, derived from an extended superformula [35, 36], enables smooth dimensional scaling and flaring, thereby providing a controlled impedance transformation that significantly enhances broadband matching performance compared to conventional probe geometries. This tailored profile mitigates abrupt discontinuities and allows fine-tuning of the transition characteristics, achieving reflection coefficients below -10 dB over a wide operational bandwidth. The integrated septum horn structure facilitates efficient dual-mode circular polarization (LHCP and RHCP), with inter-port isolation exceeding 20 dB and axial ratio maintained below 1.5 dB across the working frequency range. Additionally, the dual-feed configuration supports polarization diversity, which enhances link robustness in full-duplex satellite systems. The proposed design is validated through full-wave electromagnetic simulations, equivalent circuit modeling, and experimental measurements. A prototype is fabricated and tested, demonstrating a wide impedance bandwidth of 60.6% from 4.6 to 8.6 GHz, a stable broadside gain exceeding 15 dBi, and excellent CP performance.

The remainder of this paper is organized as follows. Section 2 presents the design methodology, including the development of the wideband coaxial-to-rectangular waveguide transition and its integration with the septum horn antenna. This section also discusses the results of a detailed parametric analysis and introduces the corresponding equivalent circuit model. Section 3 provides the measured results and compares them with the simulated data to validate the proposed design. Finally, Section 4 summarizes the main conclusions of the work. This paper's contribution is as follows:

1. A wideband coaxial-to-rectangular waveguide transition using a modified supershape probe derived from an extended superformula is proposed.

2. In [34], the supershape was applied only within the waveguide, whereas the present design integrates it into a complete stepped septum-horn antenna to realize dual circular polarization.

3. The modified superformula introduces extra degrees of freedom for adaptive impedance transformation under perturbations from the septum and flare sections.

4. The design is validated through successive stages — waveguide transition, horn integration, and equivalent-circuit modeling — showing consistent results.

5. The prototype exhibits 60.6% bandwidth, $|S_{11}| < -10$ dB, AR < 1.5 dB, and isolation > 20 dB, confirming excellent C-band performance.

2. DESIGN METHODOLOGY

2.1. Wideband Coaxial-to-Rectangular Waveguide Transition Design

Efficient coaxial-to-rectangular waveguide transitions are essential in high-frequency systems for achieving wideband impedance matching and minimizing reflection losses. Traditional designs, including stepped and tapered transitions or conventional cylindrical probes, often exhibit limited bandwidth due to abrupt geometric discontinuities and constrained design flexibility. The comparison between the two transition approaches is shown in Fig. 1. The conventional configuration, shown in Fig. 1(a), utilizes a standard cylindrical probe inserted into the waveguide. Although structurally simple, this approach exhibits narrow bandwidth performance due to abrupt impedance discontinuities. The configuration depicted in Fig. 1(b) introduces a probe geometry derived from an extended superformula (Eq. (1)). The resulting modified supershape probe incorporates controlled flaring and dimensional scaling, facilitating gradual impedance transformation between the coaxial line and the waveguide. The added flexibility of the extended formulation enables precise optimization of the transition profile, thereby improving broadband impedance characteristics.

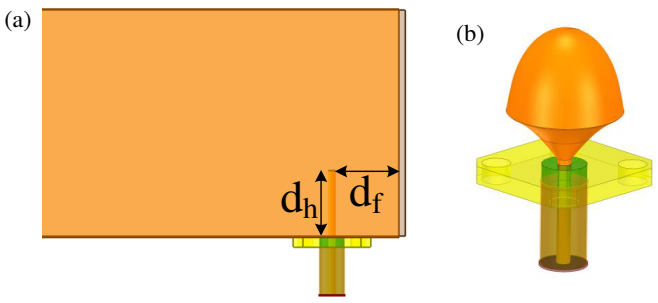

FIGURE 1. Comparison of coaxial-to-rectangular waveguide transition designs: (a) conventional probe-based transition with classical geometry, and (b) proposed transition employing a modified supershape probe for enhanced broadband performance.

The transition geometry is defined by the following polar expression:

$$r(\theta) = \left(\left|\left(\cos\left(\left(m_1\theta+\varphi\right)/4\right)\right)/a\right|^{n_2} + \left|\left(\sin\left(\left(m_2\theta\right)/4\right)\right)/b\right|^{n_3} + c\left|\left(\cos\left(\left(k\theta/2\right)\right)\right)\right|^{n_4}\right)^{-1/n_1} \quad (1)$$

The parameters m_1 and m_2 control the lobe count and rotational symmetry of the contour, while a and b scale the horizontal and vertical dimensions to match the waveguide cross section.

TABLE 1. Representative parameter sets for modified supershape geometries derived from an extended superformula.

	Shapes	m_1	m_2	n_1	n_2	n_3	n_4	a	b	ϕ	c	k
1	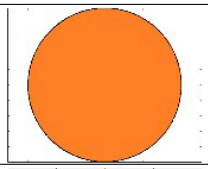	4	4	2	2	2	2	1	1	0	0	0
2	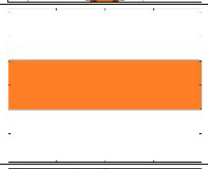	4	4	2	2	2	2	4	1	0	0	0
3	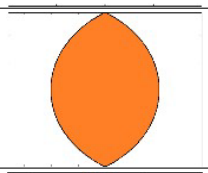	2	2	100	100	100	100	1	1	0	0	0
4	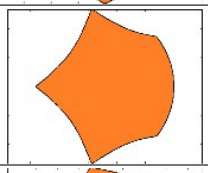	5	5	100	100	100	100	1	1	0	1	1
5	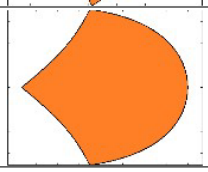	5	5	100	100	100	100	2	2	0	1	1

The exponents n_1, n_2, n_3 and n_4 govern the edge sharpness: small values yield smooth, rounded profiles, whereas large values produce flatter sides and sharper corners. The phase term φ provides a controllable rotation of the contour to introduce or remove asymmetry. Finally, the coefficient c and harmonic index k define the additional modulation term, which introduces mild flaring or ripples along the boundary and is used to fine-tune the local impedance for wideband matching. Parametric variation of these variables enables the synthesis of transition geometries suitable for wideband operation. Table 1 lists representative parameter sets used in the analysis. The parameter sets in Table 1 were obtained through a structured two-step procedure: first, m_1, m_2, a and b were constrained by the waveguide aperture and dominant TE_{10} field, while large exponents ($n_1 - n_4 = 100$) were intentionally used to realize corner-sharpened circular/rectangular limiting shapes compatible with waveguide operation. Subsequently, a multi-parameter numerical optimization based on a genetic algorithm was performed in the 4–9 GHz band, with $S_{11} < -10$ dB and smooth impedance transformation as the primary objectives. The simulated reflection coefficients, S_{11}, corresponding to the geometries listed in Table 1 are presented in Fig. 2. The results demonstrate the influence of probe shape on impedance matching performance over the frequency range of 4–9 GHz. The optimized geometry, referred to as Shape 5 in Table 1, defined by increased scaling and controlled flaring, achieves reflection coefficients below −10 dB across 4.2–8.1 GHz, meeting broadband requirements for C-band applications. This performance is attributed to smooth impedance transformation enabled by sharp-edge shaping and profile modulation. The circular and rectangular configurations exhibit acceptable impedance matching over the ranges of 4.3–5.8 GHz and 4.2–7.1 GHz, respectively, owing to their limited geometric complexity. Intermediate shapes exhibit modest improvement but fail to sustain wideband reflection performance beyond 7 GHz, with visible resonant peaks and degraded behavior. The results demonstrate that probe geometry plays a critical role in enabling wideband transitions. The extended superformula facilitates detailed shape control, enabling superior performance compared to conventional transition designs.

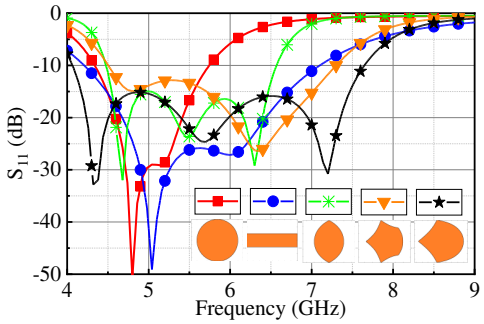

FIGURE 2. Simulated reflection coefficients (S_{11}) of the coaxial-to-rectangular waveguide transition for various modified supershape probe geometries based on parameter sets in Table 1.

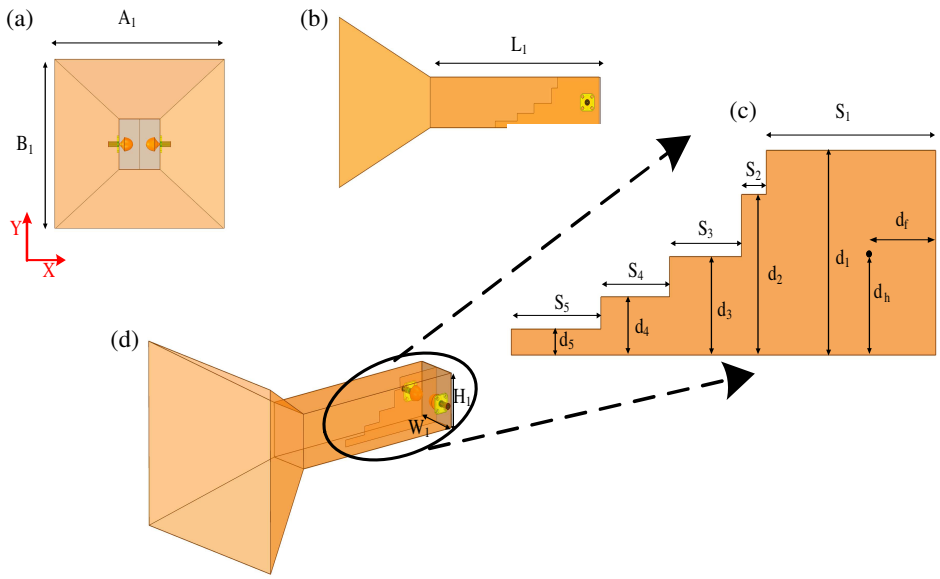

FIGURE 3. Proposed wideband septum horn comprising the modified supershape coaxial probe, rectangular waveguide, septum and flared horn: (a) front view, (b) side view, (c) enlarged view of septum steps, and (d) isometric view.

TABLE 2. Geometrical parameters of the proposed wideband septum horn antenna.

Parameter	Value (mm)	Parameter	Value (mm)	Parameter	Value (mm)
A_1	156.4	S_2	5.6	d_3	18.1
B_1	127.4	S_3	16.3	d_4	10.7
L_1	156	S_4	15.5	d_5	4.8
W_1	37.6	S_5	20.3	d_f	11
H_1	37.6	d_1	37.6	d_h	18.8
S_1	38.3	d_2	29.5		

2.2. Integration with the Septum Horn Antenna

In this section, the coaxial-to-rectangular waveguide transition developed in Section 2.1 is extended by integrating a stepped-septum horn antenna to realize a practical radiating system for satellite communication applications. While the previous section focused on achieving wideband impedance matching using a modified supershape probe derived from an extended super-formula, the present configuration incorporates a polarization conversion mechanism and a flared horn to realize dual circular polarization and enhanced radiation characteristics.

When the rectangular waveguide is excited at Port 1 with the dominant TE_{10} mode, the resulting field inside the waveguide is a horizontally polarized electric field E_X. As this E_x field encounters the vertically oriented stepped septum, it can be decomposed into a superposition of even and odd modes. In the even mode, the horizontal field E_X remains in phase across the septum; therefore, it experiences approximately 0° phase shift while passing through the stepped sections. In the odd mode, the horizontal field E_x is 180° out of phase on each side of the septum; the stepped geometry then introduces a ±90° phase shift, which creates a vertical electric-field component E_Y. The synthesis of these two orthogonal components E_X and E_Y, with a quadrature (±90°) phase difference, forms either LHCP or RHCP depending on the sign of the phase shift. Thus, the stepped septum breaks the symmetry of the rectangular waveguide, enforces controlled even-odd mode propagation, and generates the circularly polarized field at the horn aperture [37, 38].

This approach minimizes polarization mismatch and improves robustness against multipath effects. Furthermore, the use of a dual-feed configuration allows independent excitation of left-hand circular polarization (LHCP) and right-hand circular polarization (RHCP), supporting polarization diversity and enabling full-duplex communication schemes. The proposed integrated septum horn antenna is illustrated in Fig. 3. The horn aperture with dual coaxial feed ports is shown in Fig. 3(a). The side profile, highlighting the flared horn and embedded stepped septum, is depicted in Fig. 3(b). A magnified view of the septum, which introduces a controlled phase shift between orthogonal field components for circular polarization, is presented in Fig. 3(c). An isometric view of the complete assembly, illustrating the integration of the modified supershape probe, waveguide, septum, and horn, is shown in Fig. 3(d). The optimized geometrical parameters corresponding to the septum and horn design are summarized in Table 2. Initial values of the septum steps (d_1–d_5, S_1–S_5) were obtained from classical stepped-septum synthesis formulas in [37], while the waveguide size, horn aperture, and flare angle were set using

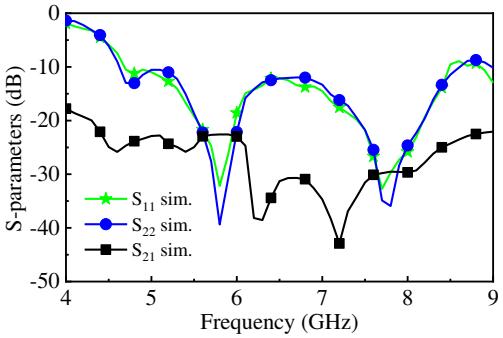

FIGURE 4. Simulated S-parameters of the proposed wideband septum horn antenna over the frequency spectrum.

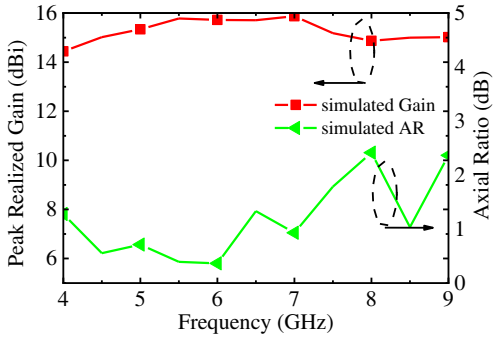

FIGURE 5. Simulated peak realized gain and axial ratio of the proposed wideband septum horn antenna across the operating frequency band.

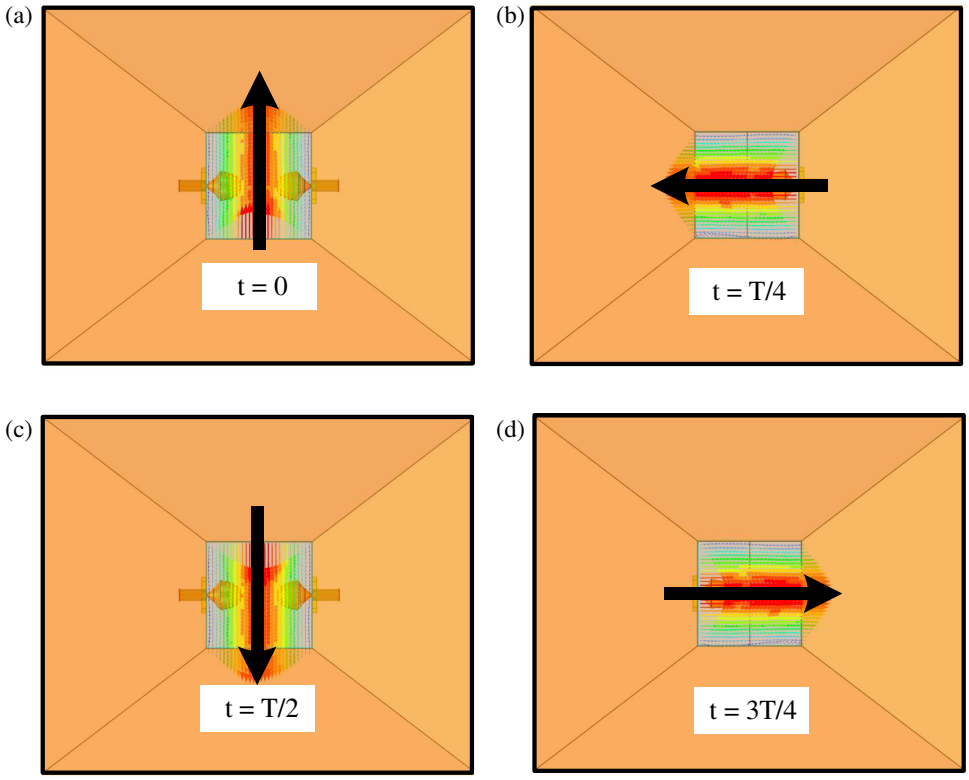

FIGURE 6. Simulated E-field distributions at 6 GHz illustrating the generation of right-hand circular polarization (RHCP) by the septum at four time phases: (a) $t = 0$, (b) $t = \mathrm{T}/4$, (c) $t = \mathrm{T}/2$, and (d) $t = 3\mathrm{T}/4$.

standard gain and phase-centre expressions for wideband horns in [39, 40]. The simulated S-parameters of the proposed wideband septum horn antenna are presented in Fig. 4. The reflection coefficients S_{11} and S_{22} are below -10 dB from 4.6 GHz to 8.6 GHz, yielding an impedance bandwidth of 60.6%. The transmission coefficient S_{21}, indicating inter-port isolation, remains below -20 dB between 4.4 GHz and 9 GHz, and below -15 dB across the 4–9 GHz range. This high isolation ensures minimal coupling between the LHCP and RHCP ports, critical for polarization purity in dual-feed systems. Moreover, the close alignment of S_{11} and S_{22} confirms port symmetry and validates the effectiveness of the balanced feed design. The simulated peak realized gain and axial ratio of the proposed wideband septum horn antenna across the 4–9 GHz band are illustrated in Fig. 5.

The antenna demonstrates stable gain characteristics, with values of 14.44 dBi at 4 GHz, 15.8 dBi at 6 GHz, 15.79 dBi at 6.5 GHz, and a maximum of 15.92 dBi at 7 GHz, before slightly decreasing to 15.02 dBi at 9 GHz. This consistent high-gain behavior confirms the efficiency of the integrated structure over the operating band. The axial ratio remains below 3 dB from 4 GHz to 9 GHz, corresponding to a 76.9% axial ratio bandwidth. Furthermore, the axial ratio is maintained below 1.5 dB within the 4–7 GHz range, covering 54.5% of the band, indicating stable circular polarization performance.

The simulated E-field distributions at 6 GHz are presented in Fig. 6 to verify the generation of right-hand circular polar-

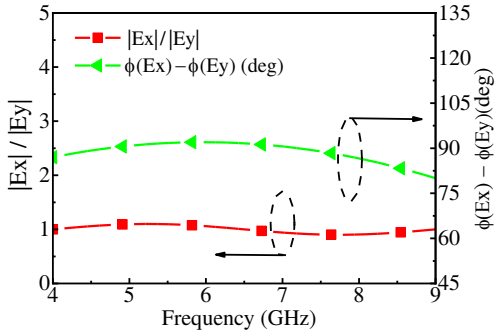

FIGURE 7. Simulated amplitude ratio $|E_x|/|E_y|$ and phase difference $\phi(E_x) - \phi(E_y)$ versus frequency for the proposed wideband septum horn antenna.

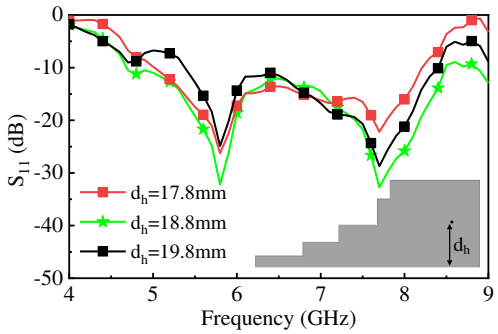

FIGURE 8. Simulated reflection coefficient for different values of the probe vertical position d_h.

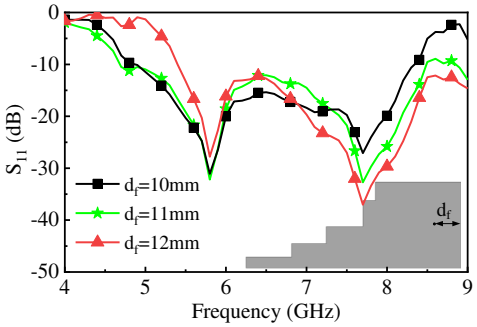

FIGURE 9. Simulated reflection coefficient for different values of the probe axial position d_f.

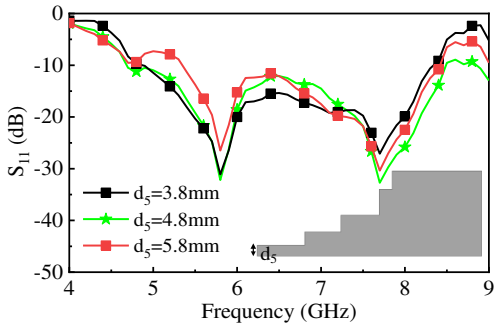

FIGURE 10. Simulated reflection coefficient for different values of the septum height d_5.

ization (RHCP) by the septum. The field patterns at four time phases, $t = 0$, T/4, T/2, and 3T/4, demonstrate the orthogonal electric field components with a uniform 90° phase shift. The observed rotational behavior confirms the effective implementation of circular polarization, validating the septum design for RHCP operation within the intended frequency band.

The simulated amplitude ratio and phase difference between the orthogonal electric field components of the proposed wideband septum horn antenna are presented in Fig. 7. The magnitude ratio $|E_x|/|E_y|$ remains between 0.9 and 1.1 across the 4–9 GHz band at boresight, indicating well-balanced field components. The corresponding phase difference $\phi(E_x) - \phi(E_y)$ remains within ±10° of 90°, satisfying the essential condition for circular polarization. The results in Figs. 5 and 6 confirm that the septum design achieves stable right-hand circular polarization over a broad frequency range, as shown by the axial ratio remaining below 3 dB and the consistent field rotation pattern.

2.3. Parametric Analysis

A parametric analysis was conducted to optimize the key design variables influencing the performance of the proposed coaxial-to-rectangular waveguide transition integrated with a septum horn antenna. The parameters considered include the vertical position d_h and axial position d_f of the coaxial probe, as well as the septum height d_5. Each parameter was varied to evaluate its impact on the reflection coefficient S_{11}, a key indicator of impedance matching.

2.4. Analysis of Probe Vertical Position d_h

The simulated reflection coefficient S_{11} for three values of the probe vertical position — 17.8 mm, 18.8 mm, and 19.8 mm — is shown in Fig. 8. The vertical position of the coaxial probe within the waveguide affects the coupling to the dominant TE_{10} mode. The configuration with d_h set to 18.8 mm produces a minimum in S_{11} near 7.7 GHz and supports a wider impedance bandwidth. In comparison, probe positions of 17.8 mm and 19.8 mm result in increased reflection and narrower bandwidths, as observed in the simulation. The vertical probe position influences the efficiency of energy transfer into the waveguide. Variations from the selected value can result in reduced excitation of the fundamental mode or excitation of higher-order modes. Selection of d_h within a defined range is therefore necessary to maintain wideband impedance matching.

2.5. Analysis of Probe Axial Position d_f

The simulated reflection coefficient S_{11} for three axial positions of the coaxial probe — 10 mm, 11 mm, and 12 mm along the waveguide — is shown in Fig. 9. The axial location of the probe affects the phase alignment and coupling efficiency between the incoming coaxial signal and the propagating mode within the waveguide structure. As observed in the figure, changes in the axial position d_f affect impedance matching and bandwidth

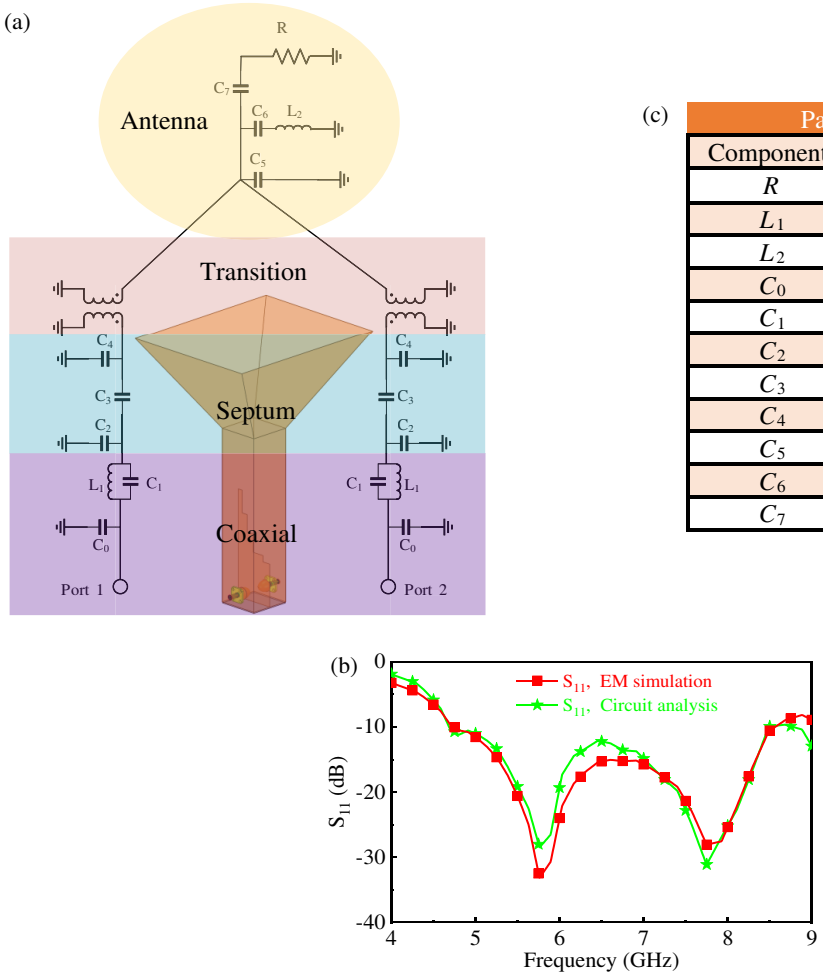

(c)

Parameters		
Component	Value	Unit
R	377	Ω
L_1	2.68	nH
L_2	17.13	nH
C_0	2.74	pF
C_1	0.12	pF
C_2	1.12	pF
C_3	1.19	pF
C_4	5.48	pF
C_5	0.78	pF
C_6	1.25	pF
C_7	0.28	pF

FIGURE 11. (a) Equivalent circuit model of the proposed wideband septum horn antenna. (b) Comparison of reflection coefficient S_{11} from full-wave electromagnetic (EM) simulation and circuit model analysis and (c) corresponding lumped element values for the equivalent circuit.

performance. The configuration with d_f set to 11 mm results in the lowest reflection near 6 GHz and 8 GHz. In comparison, the positions at 10 mm and 12 mm lead to shifted resonance frequencies and higher reflection levels, indicating less effective coupling to the dominant mode.

This parametric analysis was performed to determine the most efficient probe placement along the longitudinal axis of the waveguide. The axial position governs the effective electrical length and matching conditions, which directly influence the input reflection coefficient. Improper placement can cause standing wave formation and mismatch losses. The probe axial position was studied due to its impact on phase coherence and effective excitation

2.6. Analysis of Septum Height d_5

The simulated reflection coefficient S_{11} is shown for different values of the septum height d_5 — 3.8 mm, 4.8 mm, and 5.8 mm — is illustrated in Fig. 10. The septum height, positioned at the input region of the horn antenna, significantly affects the electromagnetic field distribution and impedance transformation between the waveguide transition and the radiating aperture. As observed, changing d_5 influences both the bandwidth and the resonance depth of the transition. The configuration with d_5 set to 4.8 mm results in lower reflection coefficients S_{11} across the operating frequency band. In comparison, septum heights of 3.8 mm and 5.8 mm produce higher S_{11} levels and reduced impedance bandwidths, indicating less effective excitation of the dominant mode. This parameter was analyzed for its effect on field symmetry and energy flow in the waveguide. Optimizing d_5 contributes to consistent dominant mode propagation and reduced mismatch.

2.7. Equivalent Circuit Design

A comprehensive understanding of the proposed wideband septum horn antenna's operating principle is facilitated by an equivalent circuit model, as depicted in Fig. 11(a). The lumped-element model provides an accurate representation by segmenting the antenna into distinct regions: the coaxial feed, septum region, transition section, and horn aperture. The coaxial feed section is modeled using the lumped elements C_0, C_1, and L_1 [41]. The capacitance C_0 represents the fundamental TEM mode of the coaxial line and is determined by the radii of the inner and outer conductors, as well as the relative permittivity of the dielectric material. The parallel combination of C_1

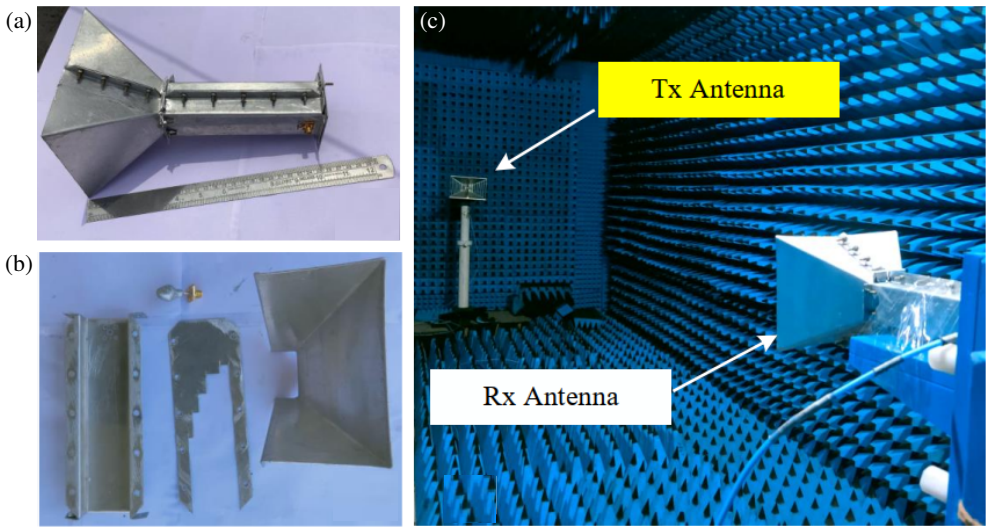

FIGURE 12. Fabricated prototype of the wideband septum horn antenna: (a) assembled view, (b) disassembled components, and (c) measurement setup inside an anechoic chamber.

and L_1 models the quarter-wavelength supershape structure located near the waveguide shorting plane. The capacitance C_1 accounts for surface coupling between the extended probe and the septum wall, and depends on the probe height, diameter, and gap spacing. The inductance L_1 corresponds to the tapered geometry of the modified supershape and is primarily governed by the probe height. The septum region, exhibiting predominantly capacitive behavior, is modeled as a lumped-element π-network comprising capacitors C_2, C_3, and C_4. Capacitors C_2 and C_4 represent the shunt capacitances to ground, while capacitor C_3 denotes the series capacitance introduced by the septum structure itself [42].

Physically, the centrally positioned aluminum septum disrupts the transverse electric fields of the dominant waveguide mode, producing localized capacitive coupling effects at its edges and across its longitudinal gap. The π-network effectively isolates the fringing field interactions represented by C_2 and C_4 from the longitudinal capacitive discontinuity modeled by C_3, thereby supporting broadband impedance matching.

The transition region from the septum-loaded waveguide to the horn antenna is represented as a transformer-coupled section [43], enabling a gradual and smooth impedance transition to maintain broadband impedance matching. Finally, the horn aperture region is modeled by lumped elements C_5, C_6, C_7, inductance L_2, and resistor R [44]. The capacitor C_5 accounts for transverse capacitive coupling across the horn's aperture, while the parallel combination of C_6 and L_2 captures frequency-dependent reactive effects associated with the horn taper. The series capacitor C_7, terminated by a resistor R with a value of 377 Ω, directly represents the horn's aperture coupling and radiation into free space. This configuration separates transverse field interactions from longitudinal radiation coupling, minimizing reflections at the horn aperture. To validate the accuracy of the proposed equivalent circuit, component parameters were extracted using Advanced Design System (ADS) and compared with full-wave electromagnetic (EM) simulations performed in HFSS. The comparison of the reflection coefficient (S_{11}) from both methods is shown in Fig. 11(b). Although minor discrepancies exist, the overall good agreement across the operating bandwidth confirms the model's validity. The lumped-element values utilized in the equivalent circuit simulation are summarized in Fig. 11(c). These parameters serve as critical references for practical antenna implementation and further optimization.

3. MEASURED RESULTS AND DISCUSSION

The fabricated prototype of the proposed wideband septum horn antenna, along with the measurement setup, is shown in Fig. 12. The assembled prototype, depicted in Fig. 12(a), exhibits a compact structure designed for C-band applications. The antenna is fabricated in two identical halves, with a metallic septum inserted between them. An exploded view showing the individual components, including the septum structure, waveguide, horn, and coaxial feed arrangement, is presented in Fig. 12(b).

The two halves, along with the septum, are mechanically secured using M2.5 screws. Provisions have been made to interface the waveguide with an SMA adaptor for ease of measurement and integration. Aluminum is used as the fabrication material due to its availability, ease of machining, and cost-effectiveness. The measurements were conducted in an anechoic chamber, as illustrated in Fig. 12(c), to ensure a controlled environment for accurate evaluation of the antenna's performance.

The S-parameter measurements of the designed antenna are carried out using the Anritsu MS2038C VNA Master vector network analyser. The simulated and experimental S-parameters, including S_{11}, S_{21}, and S_{22} are compared in Fig. 13. The measured reflection coefficient S_{11} remains below -10 dB over the 4.6–8.6 GHz range, corresponding to an impedance bandwidth of approximately 60.6%. The measured S_{11} trend aligns well with the simulation, though minor deviations ap-

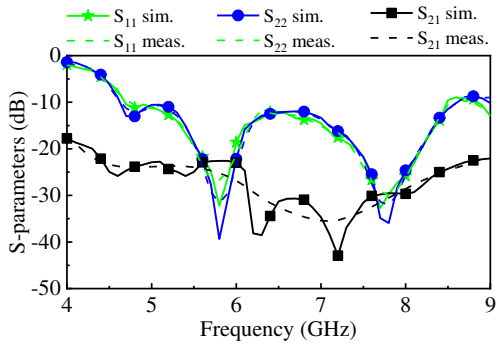

FIGURE 13. Comparison between simulated and measured S-parameters S_{11}, S_{21}, and S_{22} of the wideband septum horn antenna.

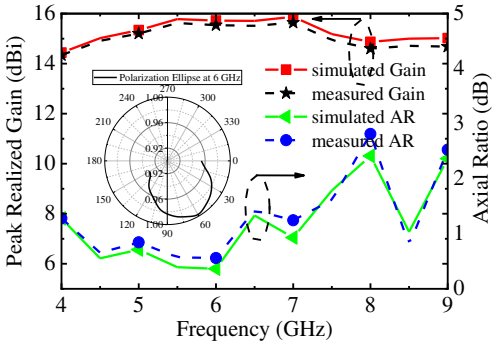

FIGURE 14. Comparison of simulated and measured peak realized gain and axial ratio (AR) for the septum horn antenna.

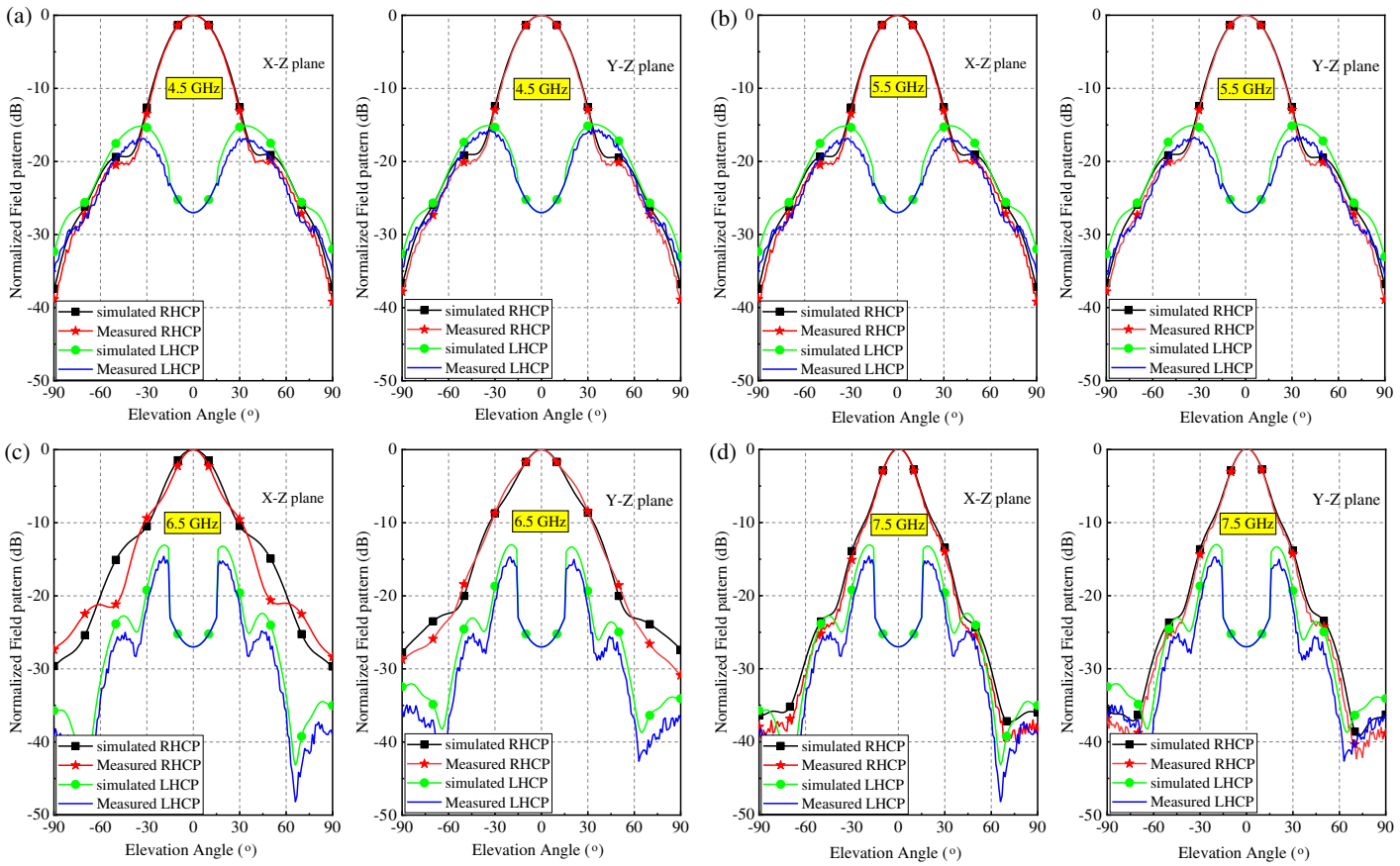

FIGURE 15. Comparison of simulated and measured radiation patterns of the proposed wideband septum horn antenna in the X–Z and Y–Z planes at: (a) 4.5 GHz, (b) 5.5 GHz, (c) 6.5 GHz, and (d) 7.5 GHz.

pear at higher frequencies, likely caused by fabrication-induced variations or connector mismatches. The close correlation between the measured and simulated S_{11} validates the antenna's impedance matching performance across the operational band.

The reflection coefficient S_{22} also exhibits strong alignment with the simulated response, confirming the accuracy of the design process. Furthermore, the isolation parameter S_{21}, which indicates coupling between Port 1 and Port 2, remains consistently below -20 dB throughout the 4.2–9 GHz range. This behaviour confirms that the antenna maintains high isolation characteristics across the intended frequency band. The frequency-dependent behavior of the antenna's simulated and measured peak realized gains and axial ratios (ARs) is shown in Fig. 14. The measured gain ranges from 14.3 dBi at 4 GHz to a peak of 15.8 dBi at 6.5 GHz, closely aligning with the simulated results. The gain remains relatively stable over the operating frequency range, with a minor decrease observed near 8 GHz. These variations can be attributed to imperfections resulting from manual fabrication processes such as cutting, drilling, and folding. The axial ratio remains under the 3 dB threshold from 4 GHz to 9 GHz in both measured and simulated responses, verifying effective circular polarization across a 76.9% bandwidth. AR measurements were obtained by incrementally rotating a

TABLE 3. Performance comparison of proposed antenna and existing designs.

Ref.	Method	Imp. BW (%)	Gain (dBi)	3 dB AR BW (%)	Isolation (dB)
[11]	Ridge/cascaded rectangular-triangular septum	66.67	10.3	64	> 20
[15]	Stepped septum, flared CWT	10	13	10	> 23
[18]	Polynomial septum	18.2	N/A	20.3	> 23
[23]	Stepped septum QRH	40	11.7	40	> 15
[25]	Twisted ridges	53	7.1	65	N/A
[28]	Ridge CWT asymmetrical-LT slot	40	15.5	40	N/A
[32]	Antipodal septum blade	40	10	37.4	> 22
This work	Stepped septum, modified-supershape-CWT	60.6	15.8	76.9	> 20

Imp. BW: Impedance bandwidth; N/A: Not available; QRH: quad-ridged horn;
CWT: coax-to-WG transition; LT: linear-tapered.

linearly polarized transmitting antenna from 0° to 150° in 10° steps and recording the corresponding signal levels at boresight. The strongest and weakest received signals were used to estimate the major and minor axes of the polarization ellipse as shown in inset of Fig. 14, from which the AR was computed. The lowest measured AR value of 0.6 dB occurs at 6 GHz, indicating robust CP performance. Slight discrepancies between measured and simulated AR values are likely due to small geometric imperfections and alignment offsets during testing.

The simulated and measured normalized far-field radiation patterns of the proposed wideband septum horn antenna in the X-Z and Y-Z planes at 4.5 GHz, 5.5 GHz, 6.5 GHz, and 7.5 GHz are shown in Fig. 15. The antenna exhibits directive main lobes with stable beam symmetry, and the measured ratio of RHCP to LHCP normalized field components at 0° is approximately 27 dB. Good agreement between simulation and measurement confirms the validity of the design and fabrication. At 4.5 GHz and 5.5 GHz, the measured and simulated normalized radiation patterns exhibit strong agreement, with consistent main-lobe widths and symmetric profiles observed in both principal planes. At 6.5 GHz, the half-power beamwidths are approximately 32° in the X-Z plane and 30° in the Y-Z plane, with radiation levels outside the main lobe suppressed below -18 dB. At 7.5 GHz, the beamwidths further narrow to approximately 29° and 28°, respectively, while the corresponding radiation levels remain below -16 dB. Across all measured frequencies, the co- and cross-polarization patterns in the X-Z and Y-Z planes are well aligned, with cross-polarization levels maintained below -25 dB within the angular sector of $\pm 60°$, confirming high polarization purity.

To highlight the contribution of the proposed design, a performance comparison with reported antennas is presented in Table 3. A ridge-loaded septum reported in [11] achieves 66.67% impedance bandwidth but a modest peak realized gain of 10.3 dBi. A stepped-septum/flared-CWT configuration in [15] yields 10% bandwidth with 13 dBi gain. A polynomial-septum profile in [18] provides inter-port isolation above 23 dB, yet is limited to 18.2% bandwidth, and no gain data are reported. A stepped-septum QRH in [23] attains 40% bandwidth, 11.7 dBi gain, and isolation exceeding 15 dB. Twisted-ridge horns in [25] and an asymmetric LT-slot with ridge CWT in [28] extend the 3-dB axial-ratio bandwidth to 65% and 40%, respectively — [25] with 53% bandwidth and 7.1 dBi gain (isolation not reported), and [28] with 40% bandwidth and 15.5 dBi gain (isolation not reported). An antipodal-septum blade in [32] demonstrates 10 dBi gain with isolation above 22 dB, while the bandwidth remains 40% with 37.4% axial-ratio bandwidth. The proposed antenna achieves 60.6% impedance bandwidth, 76.9% 3-dB axial-ratio bandwidth, 15.8 dBi peak gain, and isolation exceeding 20 dB, confirming a balanced enhancement over existing works. These results demonstrate the effectiveness of the supershape-based transition and septum-horn integration in achieving compact, wideband, and dual-polarized operation for C-band satellite applications.

4. CONCLUSION

In conclusion, this paper presents a novel wideband coaxial-to-rectangular waveguide transition integrated with a stepped septum horn antenna, tailored for C-band satellite communication applications. The transition employs a modified supershape probe derived from an extended superformula to enable smooth impedance transformation and improved broadband matching. The integration with a stepped septum horn enables efficient dual circular polarization, supporting left-hand and right-hand modes with minimal axial ratio variation and high inter-port isolation. A comprehensive design approach was adopted, encompassing parametric optimization of the probe and septum geometry, equivalent circuit modeling for analytical validation, and full-wave electromagnetic simulations. A prototype was fabricated and experimentally tested. The measured results confirm wideband performance with reflection coefficients below -10 dB over 4.6–8.6 GHz, a peak gain of 15.8 dBi, and inter-port isolation better than 20 dB. Furthermore, the axial ratio remains below 1.5 dB across 47.6% bandwidth, demonstrating strong polarization purity and radiation efficiency. A comparison with state-of-the-art designs demonstrates the en-

hanced performance and integration advantages of the proposed antenna, making it suitable for wideband satellite communication systems requiring compact form and dual circular polarization.

ACKNOWLEDGEMENT

This work is supported by the Science Engineering Research Board, Govt. of India, and Indian Space Research Organization, RAC-ISRO as sponsored research project number EEQ/2021/000588 and ISRO/RACS/IIT(BHU)/2022-23, respectively.

The authors also express their sincere gratitude to Dr. Rahul Dubey for his technical support throughout this work. His expertise, especially in experimental work and troubleshooting, was instrumental in overcoming key challenges. We are truly grateful for his time, dedication, and valuable insights.

REFERENCES

[1] Elbert, B. R., *Introduction to Satellite Communication*, Artech House, 2008.

[2] Nouri, L., L. Nkenyereye, M. A. Hafez, F. Hazzazi, M. A. Chaudhary, and M. Assaad, "A simplified and efficient approach for designing microstrip bandpass filters: Applications in satellite and 5G communications," *AEU — International Journal of Electronics and Communications*, Vol. 177, 155189, 2024.

[3] Montero, J. M., A. M. Ocampo, and N. J. G. Fonseca, "C-band multiple beam antennas for communication satellites," *IEEE Transactions on Antennas and Propagation*, Vol. 63, No. 4, 1263–1275, Apr. 2015.

[4] Lagunas, E., C. G. Tsinos, S. K. Sharma, and S. Chatzinotas, "5G cellular and fixed satellite service spectrum coexistence in C-band," *IEEE Access*, Vol. 8, 72 078–72 094, 2020.

[5] Irsigler, M., G. W. Hein, and A. Schmitz-Peiffer, "Use of C-band frequencies for satellite navigation: Benefits and drawbacks," *GPS Solutions*, Vol. 8, No. 3, 119–139, Jul. 2004.

[6] Lozano-Guerrero, A. J., F. J. Clemente-Fernandez, J. Monzo-Cabrera, J. L. Pedreno-Molina, and A. Diaz-Morcillo, "Precise evaluation of coaxial to waveguide transitions by means of inverse techniques," *IEEE Transactions on Microwave Theory and Techniques*, Vol. 58, No. 1, 229–235, Jan. 2010.

[7] Lozano-Guerrero, A. J., J. Monzó-Cabrera, J. Pitarch, F. J. Clemente-Fernández, J. Fayos-Fernández, J. L. Pedreño-Molina, A. Martínez-González, and A. Díaz-Morcillo, "Multimodal retrieval of the scattering parameters of a coaxial-to-waveguide transition," *IEEE Transactions on Microwave Theory and Techniques*, Vol. 69, No. 12, 5241–5249, Dec. 2021.

[8] Gan, T. H. and E. L. Tan, "Design of broadband circular polarization truncated horn antenna with single feed," *Progress In Electromagnetics Research C*, Vol. 24, 197–206, 2011.

[9] Shu, C., J. Wang, S. Hu, Y. Yao, J. Yu, Y. Alfadhl, and X. Chen, "A wideband dual-circular-polarization horn antenna for mmWave wireless communications," *IEEE Antennas and Wireless Propagation Letters*, Vol. 18, No. 9, 1726–1730, 2019.

[10] Zhao, Y., Z. Shen, and W. Wu, "Wideband and low-profile *H*-plane ridged SIW horn antenna mounted on a large conducting plane," *IEEE Transactions on Antennas and Propagation*, Vol. 62, No. 11, 5895–5900, 2014.

[11] Han, K., G. Wei, S. Lei, C. Qiu, and T. Qiu, "A design of broadband dual circularly polarized antenna," *International Journal of RF and Microwave Computer-Aided Engineering*, Vol. 31, No. 7, e22679, Apr. 2021.

[12] Ye, J., H. Zhang, and R. Chu, "Analysis of a new method to design a coaxial-to-rectangular waveguide transition," in *2019 International Applied Computational Electromagnetics Society Symposium — China (ACES)*, 1–2, Nanjing, China, Aug. 2019.

[13] Chen, Z. and Z. Shen, "Design of a compact phased array using 16 surface-wave antenna elements," in *2021 IEEE International Symposium on Antennas and Propagation and USNC-URSI Radio Science Meeting (APS/URSI)*, 1183–1184, Singapore,, Dec. 2021.

[14] Tako, N., E. Levine, G. Kabilo, and H. Matzner, "Investigation of thick coax-to-waveguide transitions," in *The 8th European Conference on Antennas and Propagation (EuCAP 2014)*, 908–911, The Hague, Netherlands, Apr. 2014.

[15] Sadhukhan, G. and S. Chakrabarti, "Dual feed dual circularly polarized horn antenna at Ka band," in *2019 International Conference on Range Technology (ICORT)*, 1–4, Balasore, India, 2019.

[16] Škiljo, M., Z. Blažević, and D. Poljak, "Septum feed design for right and left circular polarisation," in *2022 International Conference on Software, Telecommunications and Computer Networks (SoftCOM)*, 1–6, Split, Croatia, Sep. 2022.

[17] Addamo, G., O. A. Peverini, D. Manfredi, F. Calignano, F. Paonessa, G. Virone, R. Tascone, and G. Dassano, "Additive manufacturing of Ka-band dual-polarization waveguide components," *IEEE Transactions on Microwave Theory and Techniques*, Vol. 66, No. 8, 3589–3596, 2018.

[18] Fonseca, N. J. G. and J.-C. Angevain, "C-band septum polarizers with polynomial profile and accurate axial ratio characterization in back-to-back configuration," *IEEE Journal of Microwaves*, Vol. 2, No. 4, 678–689, 2022.

[19] Song, K. and Q. Xue, "Planar probe coaxial-waveguide power combiner/divider," *IEEE Transactions on Microwave Theory and Techniques*, Vol. 57, No. 11, 2761–2767, 2009.

[20] Piltyay, S., "Electromagnetic and bandwidth performance optimization of new waveguide polarizers with septum of a stepped-thickness type for satellite systems," *Journal of Electromagnetic Waves and Applications*, Vol. 36, No. 9, 1257–1272, 2022.

[21] Huang, Y. Q. and C. A. Liu, "Waveguide-coaxial converter based on single-ridge waveguide impedance transformation in Ka band," in *2020 3rd International Conference on Electron Device and Mechanical Engineering (ICEDME)*, 78–81, Suzhou, China, May 2020.

[22] Komarov, V. V., A. I. Korchagin, and V. P. Meschanov, "Broadband coaxial-to-waveguide transition," in *2020 International Conference on Actual Problems of Electron Devices Engineering (APEDE)*, 163–165, Saratov, Russia, Sep. 2020.

[23] Jazani, G. and A. Pirhadi, "Design of dual-polarised (RHCP/LHCP) quad-ridged horn antenna with wideband septum polariser waveguide feed," *IET Microwaves, Antennas & Propagation*, Vol. 12, No. 9, 1541–1545, 2018.

[24] Xu, Z., J. Duan, C. Hao, K. Xu, S. Chen, P. Zhao, and Y. Sun, "Compact wideband circularly polarized horn antenna with tapered slot-coupled feeding for Ku-band applications," *International Journal of RF and Microwave Computer-Aided Engineering*, Vol. 29, No. 10, e21898, Jul. 2019.

[25] Lu, K., K. W. Leung, and N. Yang, "3-D-printed circularly polarized twisted-ridge horn antenna," *IEEE Transactions on Antennas and Propagation*, Vol. 69, No. 3, 1746–1750, Mar. 2021.

[26] Shi, J., X. Yin, and W. Zhong, "Design of a K-band feed network with dual circular polarization," in *2017 Sixth Asia-Pacific Conference on Antennas and Propagation (APCAP)*, 1–3, Xi'an, China, Oct. 2017.

[27] Li, D.-Y., Y.-C. Jiao, H.-W. Yu, and Z.-B. Weng, "Wideband circularly polarized pyramidal horn antenna based on spoof surface plasmon polaritons," *IEEE Transactions on Antennas and Propagation*, Vol. 69, No. 4, 2353–2358, Apr. 2021.

[28] Yusuf, D. P., J. T. S. Sumantyo, Y. Yoshimoto, S. Gao, and K. Ito, "Dual-band circularly polarised asymmetric Linear-Tapered horn antenna for feeder of synthetic aperture radar onboard microsatellite," *IET Microwaves, Antennas & Propagation*, Vol. 19, No. 1, e70006, Jan. 2025.

[29] Leung, K. W., C.-T. Huang, Z. Fang, K. Lu, and N. Yang, "Wideband circularly polarized horn antenna with twisted ridges of gielis super-formula contour," *IEEE Transactions on Antennas and Propagation*, Vol. 73, No. 2, 1197–1202, Feb. 2025.

[30] Hossain, M. S., J. M. Lehr, A. Fierro, and E. Schamiloglu, "A wideband coaxial-to-waveguide transition devised with topology optimization," *Scientific Reports*, Vol. 15, No. 1, 1974, Jan. 2025.

[31] Yousefian, M., S. J. Hosseini, and M. Dahmardeh, "Compact broadband coaxial to rectangular waveguide transition," *Journal of Electromagnetic Waves and Applications*, Vol. 33, No. 9, 1239–1247, Apr. 2019.

[32] Cheng, X., Y. Yao, T. Yu, J. Yu, and X. Chen, "Wideband dual circularly polarized antipodal septum antenna for millimeter-wave applications," *IEEE Transactions on Antennas and Propagation*, Vol. 69, No. 6, 3549–3554, Jun. 2021.

[33] Shen, Z. and C. Feng, "A new dual-polarized broadband horn antenna," *IEEE Antennas and Wireless Propagation Letters*, Vol. 4, 270–273, 2005.

[34] Enayati, P. and D. Zarifi, "Design of a wideband coaxial-to-rectangular waveguide transition based on Supershapes," *IEEE Access*, Vol. 10, 121 924–121 929, 2022.

[35] Gielis, J., "A generic geometric transformation that unifies a wide range of natural and abstract shapes," *American Journal of Botany*, Vol. 90, No. 3, 333–338, 2003.

[36] Gielis, J. and D. Caratelli, "Computer implemented tool box systems and methods," Google Patents, US 8,818,771 B2, 2014.

[37] Chen, M. and G. Tsandoulas, "A wide-band square-waveguide array polarizer," *IEEE Transactions on Antennas and Propagation*, Vol. 21, No. 3, 389–391, May 1973.

[38] Kim, I. and Y. Rahmat-Samii, "Revisiting stepped septum circular polarizer using full-wave simulations," in *2011 IEEE International Symposium on Antennas and Propagation (APSURSI)*, 919–921, Spokane, WA, USA, 2011.

[39] Balanis, C. A., *Antenna Theory: Analysis and Design*, 3rd ed., John Wiley & Sons, 2005.

[40] Milligan, T. A., *Modern Antenna Design*, 2nd ed., John Wiley & Sons, 2005.

[41] Von Hippel, A., *Dielectrics and Waves*, MIT Press, Cambridge, MA, USA, 1954.

[42] Collin, R. E., *Foundations for Microwave Engineering*, Wiley-IEEE Press, Hoboken, NJ, USA, 2001.

[43] Ramo, S., J. R. Whinnery, and T. V. Duzer, *Fields and Waves in Communication Electronics*, John Wiley & Sons, New York, NY, USA, 1994.

[44] Harrington, R. F., *Time-Harmonic Electromagnetic Fields*, Wiley-IEEE Press, New York, NY, USA, 2001.